



LAWRENCE
LIVERMORE
NATIONAL
LABORATORY

LLNL-TR-416320

Design of a 2 MeV Compton scattering gamma-ray source for DNDO missions

F. V. Hartemann, F. Albert

August 28, 2009

Disclaimer

This document was prepared as an account of work sponsored by an agency of the United States government. Neither the United States government nor Lawrence Livermore National Security, LLC, nor any of their employees makes any warranty, expressed or implied, or assumes any legal liability or responsibility for the accuracy, completeness, or usefulness of any information, apparatus, product, or process disclosed, or represents that its use would not infringe privately owned rights. Reference herein to any specific commercial product, process, or service by trade name, trademark, manufacturer, or otherwise does not necessarily constitute or imply its endorsement, recommendation, or favoring by the United States government or Lawrence Livermore National Security, LLC. The views and opinions of authors expressed herein do not necessarily state or reflect those of the United States government or Lawrence Livermore National Security, LLC, and shall not be used for advertising or product endorsement purposes.

This work performed under the auspices of the U.S. Department of Energy by Lawrence Livermore National Laboratory under Contract DE-AC52-07NA27344.

Design of a 2 MeV Compton scattering gamma-ray source for DNDO missions

F.V. Hartemann and F. Albert

Executive summary

Nuclear resonance fluorescence-based isotope-specific detection and imaging is a powerful new technology that can enable access to new mission spaces for DNDO. Within this context, the development of advanced mono-energetic gamma ray sources plays an important role in the DNDO R&D portfolio, as it offers a faster, more precise, and safer alternative to conventional Bremsstrahlung sources. In this report, a specific design strategy is presented, along with a series of theoretical and computational tools, with the goal of optimizing source parameters for DNDO applications. In parallel, key technologies are outlined, along with discussions justifying specific choices and contrasting those with other alternatives. Finally, a complete conceptual design is described, and machine parameters are presented in detail.

Design philosophy

Precision and technology choices leading to compact sources and high effective repetition rates are the three main thrusts underlying our overall concept for a MeV-class, tunable, narrow-bandwidth (on-axis) gamma-ray source designed specifically to meet the stringent requirements of nuclear resonance fluorescence-based isotopic detection and imaging. The implications, in terms of laser and rf technologies, are that we seek highly stable, repeatable, well-characterized energy and power sources: solid-state HV modulator, diode-pumping, ultra-low phase and amplitude rf noise, minimum jitter in trigger and synchronization, as well as a drastic reduction in parasitic x-ray and gamma-ray production via dark current and Bremsstrahlung. High-gradient rf structures and fiber-based integrated laser technology are also chosen to satisfy our ultimate goal of compactness; finally, close attention to thermal and cooling issues, coupled to laser re-circulation techniques and multi-bunch linac operation are compatible with our overall design, enabling high effective repetition rates for the source (> 1 kHz). These

requirements helped guide the selection of the appropriate technology platforms, as outlined throughout this Report.

NRF and gamma-ray sources

Nuclear resonance fluorescence (NRF) is a quantum process whereby a nucleus is excited via electromagnetic coupling between a gamma-ray photon and the charge distribution of the quarks within the nucleus; after a short period of time (typically in the ps range), the nucleus relaxes back to its ground state by emitting a gamma-ray which has the same energy as the incident photon, except from a small recoil from the nucleus. The linewidth of this process is intrinsically extremely narrow, as shown in Mossbauer spectroscopy; it is Doppler broadened by Debye screening to approximately 10^{-5} - 10^{-6} fractional bandwidth. Because the energy levels depend on the exact nuclear structure, the NRF spectrum is isotope-dependent; in addition, NRF lines can be found in the energy range where photons are most penetrating, near the absorption minimum between photo-ionization and pair production, as shown in Figure 1. More specifically, strong NRF lines have been found at 1.733 MeV for ^{235}U , and 2.143 MeV for ^{239}Pu , near the absorption minimum of shielding materials, such as Pb.

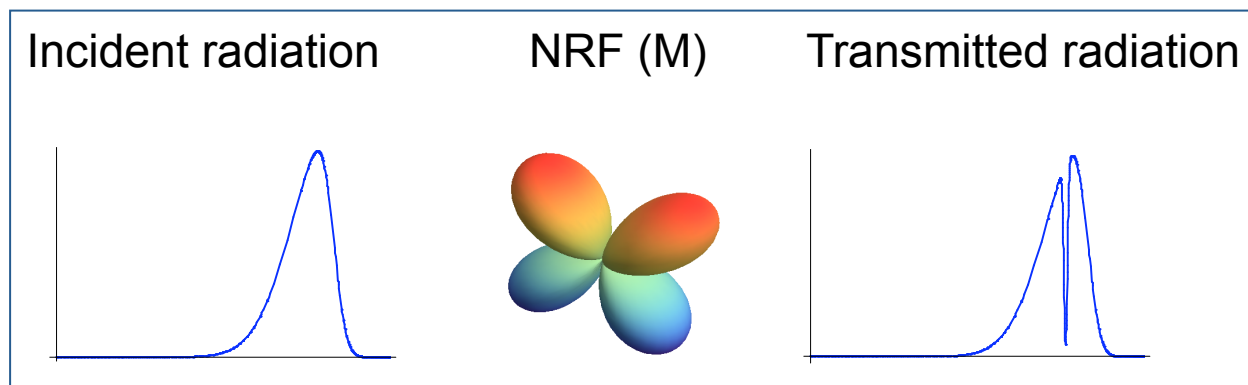


Figure 1 Schematic illustration of nuclear resonance fluorescence (NRF) excited by a Compton scattering source.

1. Introduction and background

Recent work has been performed at LLNL to demonstrate isotope-specific detection of shielded materials via nuclear resonance fluorescence using a tunable, quasi-monochromatic Compton scattering gamma-ray source operating between 0.2 MeV and

0.9 MeV photon energy. This technique is called Fluorescence Imaging in the Nuclear Domain with Energetic Radiation (or FINDER). This work has, among other things, demonstrated the detection of ^7Li shielded by Pb, utilizing gamma rays generated by a linac-driven, laser-based Compton scattering gamma-ray source developed at LLNL.

This program has also helped lay the theory and modeling foundations for isotopic imaging using NRF by benchmarking a complete suite of modeling codes against experiments, that can now be extended to address spatially-resolved, isotopic detection. The ability to produce isotope-specific images of unknown objects with deeply penetrating radiation will transform the special nuclear material (SNM) detection problem from simply identifying high optical depth cargo or high-Z materials to the unambiguous detection and verification of specific, dangerous contraband materials.

The high spectral brightness and concurrent narrow bandwidth of this novel class of light sources significantly reduces the radiological dose required for detection and largely eliminates artifacts due to small-angle elastic Compton scattering in the objects under interrogation. The highly-collimated, mono-energetic nature of the source also leads to simple detection protocols which can not only verify the presence of SNMs, but can also ascertain the absence thereof with a 99.9999% confidence level over a short interrogation time. Essentially, the phase space density of the gamma-ray beam used for interrogation or imaging is so high that discrimination against parasitic processes and backgrounds becomes both relatively simple to implement and highly effective.

The two key components of this powerful detection scheme are the Compton scattering gamma-ray source and the detection unit; LLNL possesses unique expertise in both technologies. Moreover, LLNL has assembled a team covering all specialized aspects of the system, ranging from fiber laser-driven electron photo-injectors; high-brightness, high-gradient linacs; and hyper-dispersion chirped-pulse amplification (CPA) lasers; to sub-picosecond laser-electron synchronization techniques; advanced gamma-ray modeling; and highly sensitive detectors.

The Laboratory is currently finalizing the design a tunable, narrow-bandwidth, 3rd generation mono-energetic gamma-ray (MEGa-ray) source based on new high-gradient ($> 65 \text{ MeV/m}$) X-band (11.424 GHz) rf accelerator structures capable of operating at 120 Hz, developed at SLAC (Stanford Linear Accelerator Center) that will be built in

close collaboration with SLAC; and laser technology developed for the previous T-REX (Thomson-Radiated Extreme X-Ray) source: a fiber-based photo-gun drive laser using frequency quadrupling and hyper-Michelson pulse shaping; and a 1 J, 10 ps, 10 Hz system using power amplification in Nd:YAG, operating near the Fourier transform limit with good beam quality, and utilizing proprietary LLNL hyper-dispersion stretching and compression technology. The compact accelerator will also include a custom, integrated focusing and transport lattice and interaction region designed to effectively shield parasitic x-ray production due to dark current. The facility is expected to produce gamma-ray beams at a repetition rate of up to 120 Hz, with a peak brightness of 10^{20} photons/(s x mm² x mrad² x 0.1% bandwidth).

More specifically, we seek to explore the science and technology paths required to boost the current 10 Hz mono-energetic gamma-ray technology to an effective repetition rate exceeding 1 kHz, thus potentially increasing the average source brightness by two orders of magnitude. Within the context of SNM detection and imaging, such a dramatic improvement is expected to result in much shorter data acquisition times, along with increased penetration depth, considerably cleaner statistics, and to open an R&D path to high spatial resolution isotopic imaging; in short, the proposed work is both transformational and enabling for deployable NRF interrogation with mono-energetic gamma-ray sources.

Technically, we propose two complementary approaches to boost the source average brightness; both R&D paths will increase the repetition rate of the facility by over one order of magnitude, with an ultimate overall gain of 120.

The technical means to increase the average brightness are twofold. First, by bringing the repetition rate of the lasers up from 10 Hz to 120 Hz to match the preexisting repetition rate capability of the X-band rf linac, a 12-fold increase in average flux can be immediately obtained. Second, by re-circulating the unused interaction laser light (only 10^{-10} of the energy is used in the scattering), and sending multiple electron bunches along the accelerator to better use the rf pulse width in the linac, another factor of >10 could be demonstrated. We note that the interaction laser component of this technology has already been demonstrated in terms of energetics in the RING project, and will not

be part of the proposed work; the electron beam part, on the other hand, is an important component of our near-term work.

The first research area aims to demonstrate the increase in the interaction laser repetition rate. Based on experience at LLNL with high-power diode-pumped lasers, we expect that a 1 J, 120 Hz uncompressed laser pulse can be generated with minimal thermal loading, lensing, and birefringence effects. This will require the design of a first of its kind diode-pumped, short pulse laser amplifier chain that incorporates appropriate thermal management, along with compression components that can withstand the increased average power loads. This laser, coupled with a higher repetition rate photo-injector drive laser, could then be integrated within the LLNL-funded facility to demonstrate a 12-fold increase in average gamma-ray flux.

The second research area is aimed at the development of the high-gradient, compact accelerator technology needed to support multiple, closely spaced electron bunches for operation in microburst mode. These bunches must be of exceedingly high quality to produce narrow-bandwidth gamma-rays; therefore any perturbation to a given micro-bunch, produced, for example, by electromagnetic fields generated by adjacent bunches, need to be carefully controlled. It is not known whether the existing gun designs can handle such a pulse format, or if a significantly new design will be needed. Thus, thorough modeling of beam wakefields in accelerator structures is first required, followed by experimental validation in an accelerator test stand. Beyond multi-bunch operation of a high-Q X-band rf gun, this test stand would also provide baseline measurements of dark current for various linac material processing conditions; photocathode material studies; multi-bunch acceleration in a damped, detuned X-band rf structure with a high-quality electron beam; implementation of advanced multi-bunch electron beam physics diagnostics; and evaluation of very high gradient X-band structures, both with single and multi-bunch electron pulse formats.

Within this overall context, a specific design strategy is presented in this Report, along with a series of theoretical and computational tools, with the goal of optimizing source parameters for DNDO applications. In parallel, key technologies are outlined, along with discussions justifying specific choices and contrasting those with other alternatives.

Ultimately, a complete conceptual design is described, and machine parameters are presented in detail.

More specifically, the present Report is organized as follows: in Section 2, an overview of Compton scattering theory is provided, along with more specialized sections focusing on the influence of electron beam phase space correlations upon the gamma-ray output; Section 3 is devoted to a description of interaction simulations, and the interfacing of the various design codes used for the laser and linac optimization; in Section 4, systematic parametric studies are presented, and the rationale for overall system optimization is sketched, along with machine parameters; subsequent sections focus on subsystems and the corresponding advanced technologies, including timing and synchronization in Section 5; the 0.4 GW, 11.424 GHz rf power package in Section 6; the high-brightness X-band rf gun in Section 7; the 0.25 GeV, high-gradient X-band linac in Section 8; the interaction laser system in Section 9.

2. Compton scattering theory

Different modeling strategies can be used for detailed theoretical analyses of Compton scattering; roughly speaking, these fall into four main categories: plane wave models and three-dimensional theories; and particle versus wave models. The simplest approach consists in using the Lorentz force equation to describe the electron dynamics, coupled to the radiation formula, thus describing linear Thomson scattering; linear Compton scattering can be modeled by using the Klein-Nishina differential scattering cross-section and the Compton formula; three-dimensional effects can be added by considering incoherent summations over the electron beam phase space, along with electromagnetic field models, such as the paraxial approximation or Gaussian-Hermite modes. We also note that the addition of an ad-hoc recoil-like term to the electron dynamics can be used to model recoil within the Thomson formalism. Nonlinear effects, while easily described in classical (Thomson), or semi-classical terms, are more difficult to handle via the scattering cross-section formalism, and require the introduction of multi-photon cross-sections together with multiple incident phase space integrations. In terms of wave and particle models, one can first consider the radiation formula: the electron motion is Fourier transformed over time; chirp and

other laser correlations can be accounted for, and nonlinear effects can be included straightforwardly; however, neither recoil (both in frequency and cross-section), nor spin are described. Using the differential cross-section, on the other hand, allows for the retrieval of temporal information, and accounts for recoil and spin. Within this context, correlated laser phase spaces require using the Wigner distribution approach, and nonlinear effects are much more difficult to implement.

Finally, we also note that Monte-Carlo simulations offer a powerful alternative approach to describing three-dimensional and nonlinear effects, although one important challenge remains the appropriate mapping of the incident electromagnetic field distribution onto the corresponding photon phase space.

2.1. Differential brightness

In this section, the differential brightness is defined, beginning with the number of photons scattered per unit 4-volume:

$$\frac{d^4 N}{d\mathbf{x}^3 cd t} = \frac{\sigma}{ec} j_\mu \Phi^\mu, \quad (1)$$

where $j_\mu = \rho c u_\mu / \gamma$ is the electron bunch 4-current density, expressed in terms of the charge density, $\rho = n_e e$, and the 4-velocity, $u_\mu = dx_\mu / cd\tau = (\gamma, \mathbf{u}) = \gamma(1, \boldsymbol{\beta})$; and $\Phi_\mu = n_\lambda k_\mu / k$ is the laser pulse 4-flux, expressed in terms of photon density and 4-wavenumber. Using these definitions in Equation (1) yields:

$$\frac{d^4 N}{d\mathbf{x}^3 cd t} = \sigma n_e n_\lambda \frac{u_\mu k^\mu}{\gamma k} = \sigma n_e n_\lambda \left(1 - \frac{\boldsymbol{\beta} \cdot \mathbf{k}}{k} \right). \quad (2)$$

Taking successive derivatives of this quantity with respect to parameters describing the phase spaces of the incident and scattered radiation, as well as the electron beam

yields the differential brightness. Introducing the incident light-cone variable, $\kappa = u_\mu k^\mu$, and differentiating with respect to the scattered radiation solid angle, one first obtains:

$$\frac{d^5 N}{d\Omega d\mathbf{x}^3 c dt} = \frac{d\sigma}{d\Omega} n_e n_\lambda \frac{\kappa}{\gamma k}. \quad (3)$$

In the linear regime, defined by the inequality $-A_\mu A^\mu (\epsilon / m_0 c)^2 \ll 1$, where A_μ is the incident radiation 4-potential, the scattered radiation wavenumber, q_C , is given by the Compton formula; extensions to the nonlinear regime can also be readily defined; within this context, the scattered spectral density is:

$$\frac{d^6 N}{dq d\Omega d\mathbf{x}^3 c dt} = \frac{d\sigma}{d\Omega} \delta(q - q_C) n_e n_\lambda \frac{\kappa}{\gamma k}. \quad (4)$$

At this point, the phase space densities of the incident electrons and photons can be introduced to yield the differential brightness:

$$\frac{d^{12} N}{dq d\Omega d\mathbf{x}^3 c dt d\mathbf{u}^3 d\mathbf{k}^3} = \frac{d\sigma}{d\Omega} \delta(q - q_C) \frac{d^3 n_e}{d\mathbf{u}^3} \frac{d^3 n_\lambda}{d\mathbf{k}^3} \frac{\kappa}{\gamma k}. \quad (5)$$

This quantity correlates the 3 phase space densities characterizing the Compton scattering interaction: the incident radiation, with the conjugate 4-vectors x_μ and k_μ , and the constraint $k_\mu k^\mu = 0$; the incident electrons, with the conjugate 4-vectors x_μ and $p_\mu = m_0 c u_\mu$, and the constraint $u_\mu u^\mu = 1$; and the scattered radiation with the conjugate 4-vectors x_μ and q_μ , and the constraint $q_\mu q^\mu = 0$. In the case of the scattered radiation, the scattered 4-wavenumber can be expressed more explicitly in terms of spherical coordinates, with $q_\mu = q(1, \sin\theta \cos\phi, \sin\theta \sin\phi, \cos\theta)$, and Equation (5) reads:

$$\frac{d^{13}N}{dq \sin\theta d\theta d\varphi d\mathbf{x}^3 c dt d\mathbf{u}^3 d\mathbf{k}^3} = \frac{d^2\sigma}{\sin\theta d\theta d\varphi} \delta(q - q_c) \frac{d^3n_e}{d\mathbf{u}^3} \frac{d^3n_\lambda}{d\mathbf{k}^3} \frac{\kappa}{\gamma k}. \quad (6)$$

To summarize, there are 3 independent degrees of freedom for the momenta of the incident and scattered photons, and the incident electrons, and 4 common space-time coordinates, yielding a total of 13 differential quantities. To obtain the brightness in the conventional units of photons scattered per unit time, surface, solid angle, and wavenumber, Equation (5) must be integrated over the momentum space of the incident electrons and photons, and along the radiation axis, taking into account retardation. For example, on-axis radiation is characterized by the peak brightness given by:

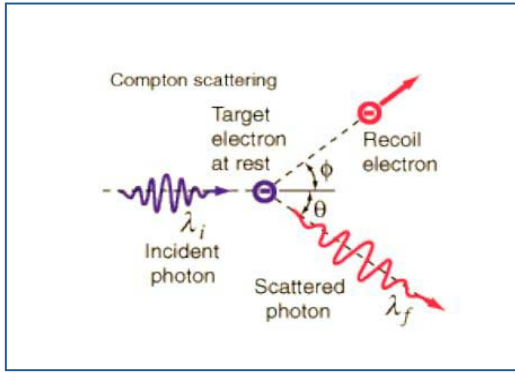
$$\begin{aligned} & \frac{d^6N}{dq \sin\theta d\theta d\varphi dx dy dt_d} \\ &= \iiint_{\mathbb{R}^3} d^3\mathbf{u} \iiint_{\mathbb{R}^3} d^3\mathbf{k} \int_{-\infty}^{+\infty} dz \int_{-\infty}^{+\infty} c dt \delta\left(t_d - t + \frac{z - z_d}{c}\right) \frac{d^2\sigma}{\sin\theta d\theta d\varphi} \delta(q - q_c) \frac{d^3n_e}{d\mathbf{u}^3} \frac{d^3n_\lambda}{d\mathbf{k}^3} \frac{\kappa}{\gamma k}. \end{aligned} \quad (7)$$

This quantity is easily translated into synchrotron units by considering a 1 mm² surface ($\Delta x \Delta y = 10^{-6} \text{ m}^2$), a 1 mrad² solid angle ($\Delta\Omega = 10^{-6} \text{ rad}^2$), and 0.1% bandwidth, corresponding to $\Delta q = q \times 10^{-3}$. It is important to note that, while the concept of phase space density is quite straightforward and well-established for the electron beam, its incident photon pulse counterpart is, in general, poorly defined. The Wigner distribution formalism can help better and more formally describe the phase space density of the incident radiation, and simple cases, such as Fourier transform-limited, and diffraction-limited beams can be modeled by uncorrelated distributions taking the form of products of functions of conjugate variables; nonetheless, a general formalism is currently lacking.

2.2. Compton formula

For brevity, QED units are now used unless otherwise specified: charge is measured in units of the electron absolute charge, e ; mass in units of the electron rest mass, m_0 ; length in units of the reduced electron Compton wavelength, $\lambda_c = \hbar / m_0 c$; and time in units of λ_c / c . Energy-momentum conservation requires that:

$$u_\mu + k_\mu = v_\mu + q_\mu. \quad (8)$$



Here, u_μ and v_μ are the initial and scattered electron 4-velocities, while k_μ and q_μ are the incident and scattered 4-wavenumbers, respectively. The 4-velocities are normalized, with $u_\mu u^\mu = 1 = v_\mu v^\mu$, and the photon mass shell condition, or dispersion relation, implies that

Figure 2 Compton Scattering

$k_\mu k^\mu = 0 = q_\mu q^\mu$; using these conditions in conjunction with Equation (8) allows for the elimination of the scattered electron 4-velocity, v_μ , and results in the sought-after relation between the initial and final photon states:

$$q_\mu (u^\mu + k^\mu) = k_\mu u^\mu. \quad (9)$$

Equation (9) can be also written in a slightly different manner by introducing the incident and scattered light-cone variables, $\kappa = u_\mu k^\mu$, and $\lambda = u_\mu q^\mu$, respectively:

$$\kappa - \lambda = k_\mu q^\mu. \quad (10)$$

Finally, in regular units and 3-vector form; $u_\mu = (\gamma, \mathbf{u})$; $q_\mu = q_C (1, \mathbf{n})$, where \mathbf{n} is the unit vector along the direction of observation; and $k_\mu = (k, \mathbf{k})$; this yields the well-known Compton formula:

$$\frac{q_C}{k} = \frac{\gamma - \mathbf{u} \cdot (\mathbf{k} / k)}{\gamma - \mathbf{n} \cdot \mathbf{u} + \lambda_C (k - \mathbf{n} \cdot \mathbf{k})}. \quad (11)$$

As mentioned earlier, this approach is valid in the linear regime; nonlinear effects are discussed in a later section.

2.3. Klein-Nishina formula

At this point, a covariant expression for the scattering differential cross-section is required in order to obtain a frame-independent description of the scattering process. Generally, the Klein-Nishina cross-section is expressed in a reference frame where the electron is initially at rest; unfortunately, this expression is far from being manifestly covariant, and its generalization is difficult, as noted by Bhatt *et al.*, who provided a derivation from QED yielding both the spin-dependent and the spin-independent components of the cross-section. For the purpose of this paper, since most applications of interest use spin unpolarized electron beams, only the spin-independent part will be considered; in QED units, it reads:

$$\frac{d\sigma}{d\Omega} = \frac{\alpha^2}{2} \left(\frac{q}{\kappa} \right)^2 \left\{ \frac{1}{2} \left(\frac{\kappa}{\lambda} + \frac{\lambda}{\kappa} \right) - 1 + 2 \left[\varepsilon_\mu \pi^\mu - \frac{(\varepsilon_\mu u^\mu)(\pi_\mu v^\mu)}{\kappa} + \frac{(\varepsilon_\mu v^\mu)(\pi_\mu u^\mu)}{\lambda} \right]^2 \right\}. \quad (12)$$

Note that the quantity $d\sigma / q^2 d\Omega$ is manifestly covariant, since κ and λ are both Lorentz-invariant scalars. Here, α is the fine structure constant; $v_\mu = u_\mu + k_\mu - q_\mu$ is the electron 4-momentum after the interaction; ε_μ , and π_μ are the incident and scattered 4-

polarizations, which can be expressed in terms of the 4-potential as $\varepsilon_\mu = A_\mu / \sqrt{A_\mu A^\mu}$. The term containing the polarization 4-vectors reduces to the Thomson scattering cross-section if $\tilde{\lambda}_c \rightarrow 0$.

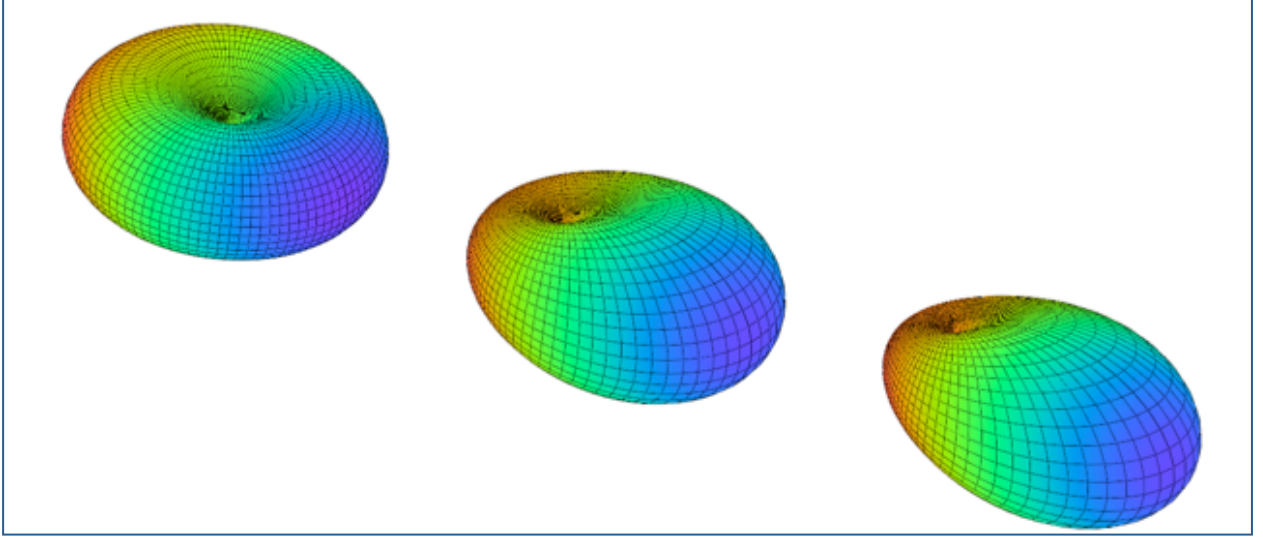


Figure 3 Klein-Nishina differential scattering cross-section for 3 different values of the recoil parameter: $\tilde{\lambda}_c k = 0, 0.5, 1$.

2.4. Dose

In this section, the space-time overlap between the incident laser pulse and electron beam is considered to determine the total scattered radiation dose. The spatial and temporal incident photon density distribution is described by Gaussians within the paraxial approximation, which is valid for most experimental situations; specifically, the ratio of the transverse to axial wavenumber satisfies the condition $(k_\perp / k_\parallel)^2 \ll 1$. To further simplify our approach, cylindrical foci are considered:

$$n_\lambda = \frac{N_\lambda}{\sqrt{\frac{\pi}{2}} w_0^2 z_0 \bar{\Delta}} \frac{1}{1 + \bar{z}^2} \exp \left[-2 \left(\frac{\bar{t} - \bar{z}}{\bar{\Delta}} \right)^2 - 2 \frac{\bar{r}^2}{1 + \bar{z}^2} \right], \quad (13)$$

Here, z and t are normalized to the Rayleigh range, $z_0 = \pi w_0^2 / \lambda_0$, and r is normalized to the focal spot size, w_0 ; $\bar{\Delta} = c\Delta t / z_0$, and N_λ is the number of incident photons. The electron beam can be described in a similar fashion:

$$n_e = \frac{N_e}{\sqrt{\pi}^3 w_0^2 z_0 \bar{\Delta} \bar{r}_b^2} \frac{1}{1 + \bar{k}^2 \bar{z}^2} \exp \left[- \left(\frac{\bar{t} - \beta \bar{z}}{\bar{\Delta}} \right)^2 - \frac{\bar{r}^2}{\bar{r}_b^2 (1 + \bar{k}^2 \bar{z}^2)} \right]. \quad (14)$$

The normalized electron beam focal radius $\bar{r}_b = r_b / w_0$, the normalized pulse duration $\bar{\Delta} = c\Delta t / z_0$, and the normalized inverse beta function, $\bar{k} = \frac{\varepsilon_n}{\gamma r_b^2} z_0$, where ε_n is the normalized beam emittance.

The dose can be calculated by integrating Equation (2):

$$\begin{aligned} N &= \sigma \frac{u_\mu k^\mu}{\gamma k} w_0^2 z_0^2 \int_0^\infty 2\pi \bar{r} d\bar{r} \int_{-\infty}^{+\infty} d\bar{t} \int_{-\infty}^{+\infty} n_e n_\lambda d\bar{z} \\ &= \frac{\sigma}{w_0^2} \frac{u_\mu k^\mu}{\gamma k} \frac{N_e N_\lambda}{\left(\frac{\pi}{\sqrt{2}}\right)^3 \bar{\Delta} \bar{r}_b^2} \int_0^\infty \exp \left[- \frac{\bar{r}^2}{\bar{r}_b^2 (1 + \bar{k}^2 \bar{z}^2)} - \frac{2\bar{r}^2}{1 + \bar{z}^2} \right] 2\pi \bar{r} d\bar{r} \iint_{\mathbb{R}^2} \frac{\exp \left[-2 \left(\frac{\bar{t} - \beta \bar{z}}{\bar{\Delta}} \right)^2 - \left(\frac{\bar{t} - \beta \bar{z}}{\bar{\Delta}} \right)^2 \right]}{(1 + \bar{k}^2 \bar{z}^2)(1 + \bar{z}^2)} d\bar{t} d\bar{z}. \end{aligned} \quad (15)$$

These are standard integrals; the result is:

$$\begin{aligned} N &= \sqrt{\frac{8}{\pi}} \frac{\sigma}{w_0^2} \frac{u_\mu k^\mu}{\gamma k} N_e N_\lambda \frac{e^{\sqrt{\frac{2l(1-\beta)^2}{mn}}} \left\{ \Phi \left[\sqrt{\frac{2l(1-\beta)^2}{mn}} \right] + 1 \right\}}{\sqrt{lmn}}; \\ l &= 1 + 2\bar{r}_b^2, \quad m = 1 + 2\bar{k}^2 \bar{r}_b^2, \quad n = 2\bar{\Delta}^2 + \bar{\Delta}^2. \end{aligned} \quad (16)$$

$\sigma = 8\pi r_0^2 / 3$ is the total scattering cross-section, and $r_0 = e^2 / 4\pi\epsilon_0 m_0 c^2$ is the classical electron radius; in QED units $\sigma = 8\pi\alpha^2 / 3$, since $r_0 = \alpha \lambda_c$. Φ is the error function.

2.5. Retardation

To derive the temporal shape of the scattered radiation pulse on a detector, retardation must be taken into account. Returning to Equation (2), and using the units defined above,

$$\frac{d^4 N}{2\pi \bar{r} d\bar{r} d\bar{z} d\bar{t}} = \sigma n_e n_\lambda w_0^2 z_0^2 \frac{u_\mu k^\mu}{\gamma k}. \quad (17)$$

Formally, the flux on a detector positioned on-axis is given by:

$$\frac{dN}{d\bar{t}_d} = \int_0^\infty 2\pi \bar{r} d\bar{r} \int_{-\infty}^{+\infty} \int_{-\infty}^{+\infty} \sigma n_e n_\lambda w_0^2 z_0^2 \frac{u_\mu k^\mu}{\gamma k} \delta(\bar{t} - \bar{t}_d + \bar{z}) d\bar{z} d\bar{t}. \quad (18)$$

Here we have used the fact that the flux is independent from the normalized position \bar{z}_d of the detector. The radial and temporal integrals are readily performed to obtain:

$$\frac{d^2 N}{d\bar{t}_d d\bar{z}} = \frac{\sqrt{8}}{\pi^2} \frac{\sigma}{w_0^2} \frac{u_\mu k^\mu}{\gamma k} \frac{N_e N_\lambda}{\bar{\Lambda} \bar{\Delta}} \frac{\exp \left\{ -\frac{[\bar{t}_d - \bar{z}(1+\beta)]^2}{\bar{\Lambda}^2} - \frac{2(\bar{t}_d - 2\bar{z})^2}{\bar{\Delta}^2} \right\}}{1 + \bar{z}^2 + 2\bar{r}_b^2 (1 + \bar{k}^2 \bar{z}^2)}. \quad (19)$$

While the integral over \bar{z} cannot be performed analytically, an excellent approximation can be obtained using the product of the Gaussian $\exp \left[-(\bar{t}_d / \bar{\Lambda})^2 \right]$ by a Lorentzian of unknown width, $\left[1 + (\bar{t}_d / x\bar{\Lambda})^2 \right]^{-1}$. First, the amplitude is easily obtained by integrating Equation (19) at the detector time $\bar{t}_d = 0$:

$$\begin{aligned}
\left. \frac{dN}{dt_d} \right|_{\bar{t}_d=0} &= \frac{\sqrt{8}}{\pi^2} \frac{\sigma}{w_0^2} \frac{u_\mu k^\mu}{\gamma k} \frac{N_e N_\lambda}{\bar{\Lambda} \bar{\Delta}} \int_{-\infty}^{+\infty} \frac{\exp \left\{ \bar{z}^2 \left[\frac{(1+\beta)^2}{\bar{\Lambda}^2} + \frac{8}{\bar{\Delta}^2} \right] \right\}}{1 + \bar{z}^2 + 2\bar{r}_b^2 (1 + \bar{k}^2 \bar{z}^2)} d\bar{z}, \\
&= \frac{\sqrt{8}}{\pi} \frac{\sigma}{w_0^2} \frac{u_\mu k^\mu}{\gamma k} \frac{N_e N_\lambda}{\bar{\Lambda} \bar{\Delta}} \frac{\exp \left[\frac{8\bar{\Lambda}^2 + (1+\beta)\bar{\Delta}^2}{\bar{\Lambda}^2 \bar{\Delta}^2} \frac{l}{m} \right] \left[\Phi \sqrt{\frac{8\bar{\Lambda}^2 + (1+\beta)\bar{\Delta}^2}{\bar{\Lambda}^2 \bar{\Delta}^2} \frac{l}{m}} - 1 \right]}{\sqrt{lm}}.
\end{aligned} \tag{20}$$

It should also be noted that the dose must be recovered upon integration over the detector time:

$$N = \left. \frac{dN}{dt_d} \right|_{\bar{t}_d=0} \int_{-\infty}^{+\infty} \frac{e^{-(\bar{t}_d / \bar{\Lambda})^2}}{1 + (\bar{t}_d / x\bar{\Lambda})^2} d\bar{t}_d. \tag{21}$$

The integral yields $\pi x \bar{\Lambda} e^{x^2} [\Phi(x) - 1]$; using Equation (20), one ends up with:

$$N = \sqrt{8} \frac{\sigma}{w_0^2} \frac{u_\mu k^\mu}{\gamma k} \frac{N_e N_\lambda}{\bar{\Delta}} \frac{\exp \left[\frac{8\bar{\Lambda}^2 + (1+\beta)\bar{\Delta}^2}{\bar{\Lambda}^2 \bar{\Delta}^2} \frac{l}{m} \right] \left[\Phi \sqrt{\frac{8\bar{\Lambda}^2 + (1+\beta)\bar{\Delta}^2}{\bar{\Lambda}^2 \bar{\Delta}^2} \frac{l}{m}} - 1 \right]}{\sqrt{lm}} x e^{x^2} [\Phi(x) - 1]. \tag{22}$$

This is to be compared with the dose, as calculated in Equation (16); to this end, the ultra-relativistic case is considered, where $\beta \rightarrow -1$:

$$x e^{x^2} [\Phi(x) - 1] = \frac{\bar{\Delta}}{\sqrt{n} \sqrt{\pi}} \frac{\left[\Phi \left(\sqrt{\frac{8l}{mn}} \right) - 1 \right]}{\left[\Phi \left(\sqrt{\frac{8l}{\bar{\Delta}^2 m}} \right) - 1 \right]} \exp \left[8 \frac{l}{m} \left(\frac{1}{n} - \frac{1}{\bar{\Delta}^2} \right) \right]. \tag{23}$$

The solution to Equation (23) defines the sought-after Lorentzian width, $x\bar{\Lambda}$.

2.6. Peak brightness: laser transform limited (uncorrelated) case

In this section, the peak brightness is first derived in the case where the absence of phase space correlations allows for the decoupling of the space-time and energy-momentum integrals:

$$\frac{d^3 n_e}{d\mathbf{u}^3} \frac{d^3 n_\lambda}{d\mathbf{k}^3} = n_e(x_\mu) \tilde{n}_e(u_\mu) n_\lambda(x_\mu) \tilde{n}_\lambda(k_\mu). \quad (24)$$

To further simplify derivations, the laser pulse is modeled by a Gaussian spectrum in Fourier space:

$$\tilde{n}_\lambda(k_\mu) = \frac{1}{\sqrt{2\pi\Delta k}} \exp\left[-\left(\frac{k-k_0}{\Delta k}\right)^2\right] \delta(\mathbf{k}_\perp); \quad (25)$$

the electron bunch phase space is modeled in terms of its normalized emittance, with $\Delta u_\perp = \varepsilon_n / r_b$,

$$\tilde{n}_e(u_\mu) = \frac{1}{\pi\Delta u_\perp^2} \exp\left[-\left(\frac{u_\perp}{\Delta u_\perp}\right)^2\right] \delta(\gamma - \gamma_0). \quad (26)$$

The quantity to be integrated over the laser spectrum and the electron bunch transverse velocity distribution is:

$$\frac{1}{\sqrt{\pi\Delta k\pi u_\perp^2}} \int_0^\infty e^{-u_\perp^2/\Delta u_\perp^2} 2\pi u_\perp du_\perp \int_{-\infty}^{+\infty} \frac{d\sigma}{d\Omega} \delta[q - q_c(k)] \frac{\kappa}{\gamma_0 k} \exp\left[-\left(\frac{k-k_0}{\Delta k}\right)^2\right] dk. \quad (27)$$

The spectral integral can be performed by considering the Dirac delta function, and evaluating its k -pole:

$$k_1 = q \frac{\gamma - u_x \sin \theta \cos \phi - u_y \sin \theta \sin \phi - u_z \cos \theta}{\gamma - u_z + q \tilde{\lambda}_c (\cos \theta - 1)}. \quad (28)$$

Equation (27) now reads:

$$\frac{1}{\sqrt{\pi} \Delta k \pi u_{\perp}^2} \int_0^{\infty} \left[\frac{d\sigma}{d\Omega} \frac{\kappa}{\gamma_0 k} \frac{e^{-(k-k_0)^2 / \Delta k^2}}{|\partial_k q_c(k)|} \right]_{k=k_1} e^{-u_{\perp}^2 / \Delta u_{\perp}^2} 2\pi u_{\perp} du_{\perp}. \quad (29)$$

Now specializing the analysis to on-axis radiation by setting $\theta = \pi$, the quantity to be integrated over the laser bandwidth can be Taylor-expanded by assuming small values of the transverse momenta and energy spread. This calculation leads to a Gaussian-error function spectral shape, where the high-energy cutoff reflects the kinematics of the interaction, while emittance contributes a low-energy tail.

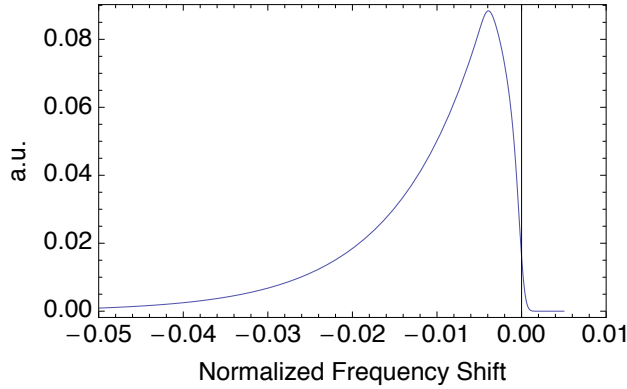


Figure 4 On-axis brightness, arbitrary units, in the case of a correlated electron beam where $\gamma = \gamma_0 \cos \phi_{rf}$. This type of correlation is typical of rf linacs.

2.7. Modified radiation formula

As mentioned above, recoil can play a role in high-energy gamma-ray production, especially when considering narrow-bandwidth operation, which is highly desirable for DNDO missions. In this sub-section, a simple method is presented, whereby the well-known classical radiation formula is modified to include recoil.

The radiation from a classical point electron is described by the number of photons scattered per unit frequency and per unit solid angle:

$$\frac{d^2 N_s}{d\omega_s d\Omega_s} = \frac{\alpha \omega_s}{4\pi^2} \left| \mathbf{n}_s \times \int_{-\infty}^{+\infty} \mathbf{u}(\tau) \exp[-ik_\mu^s x^\mu(\tau)] d\tau \right|^2, \quad (30)$$

where α is the fine structure constant, $k_\mu^s = \omega_s (1, \mathbf{n}_s)$ is the scattered 4-wavenumber, $u_\mu = (\gamma, \mathbf{u}) = dx_\mu / d\tau$ is the electron 4-velocity, and $x_\mu(\tau)$ is its 4-position.

In the case of a plane wave in the linear regime, the 4-velocity is:

$$u_\mu(\phi) = u_\mu^0 + A_\mu(\phi) - k_\mu^i \frac{A_\nu u_0^\nu}{k_\nu^i u_0^\nu}, \quad \phi = -k_\mu^i x^\mu, \quad (31)$$

where u_μ^0 is the initial 4-velocity, A_μ is the 4-potential of the plane wave, $k_\mu^i = (\omega_i, \mathbf{k}_i)$ is the 4-wavenumber of the incident plane wave, and ϕ is the phase. In addition, the so-called light-cone variable, $\kappa = d\phi / d\tau$, is conserved:

$$\frac{d\phi}{d\tau} = -k_\mu^i \frac{dx^\mu}{d\tau} = -k_\mu^i u^\mu = -k_\mu^i u_0^\mu. \quad (32)$$

It then proves useful to change variables in the radiation integral:

$$\frac{d^2 N_s}{d\omega_s d\Omega_s} = \frac{\alpha \omega_s}{4\pi^2} \left| \frac{\mathbf{n}_s}{k_\mu^i u_0^\mu} \times \int_{-\infty}^{+\infty} \left[\mathbf{A}(\phi) - \mathbf{k}_i \frac{A_\nu u_0^\nu}{k_\nu^i u_0^\nu} \right] \exp[-ik_\mu^s x^\mu(\phi)] d\phi \right|^2. \quad (33)$$

Note that the dc spectral component driven by u_μ^0 has been dropped. Further simplification occurs in the case of a monochromatic wave, with $\mathbf{A}(\phi) = \mathbf{A}_0 e^{-i\phi}$:

$$\frac{d^2 N_s}{d\omega_s d\Omega_s} = \frac{\alpha \omega_s}{4\pi^2} \left| \frac{\mathbf{n}_s}{k_\mu^i u_0^\mu} \times \left(\mathbf{A}_0 + \mathbf{k}_i \frac{\mathbf{A}_0 \cdot \mathbf{u}_0}{k_\mu^i u_0^\mu} \right) \int_{-\infty}^{+\infty} \exp \left\{ -i \left[\phi + k_\mu^s x^\mu(\phi) \right] \right\} d\phi \right|^2. \quad (34)$$

At this point, an expression for the electron trajectory, parameterized by phase, is required; for a vanishingly small A_0 , which is appropriate to model a classical photon-like excitation, one can use the ballistic component of the trajectory:

$$\frac{dx_\mu}{d\phi} = \frac{dx_\mu}{d\tau} \frac{d\tau}{d\phi} = \frac{u_\mu}{-k_\mu^i u_0^\mu} \simeq \frac{u_\mu^0}{-k_\mu^i u_0^\mu}, \quad x_\mu(\phi) \simeq x_\mu^0 - \frac{u_\mu^0 \phi}{k_\mu^i u_0^\mu}. \quad (35)$$

The radiation formula now takes the form of the Fourier transform of a delta-function:

$$\frac{d^2 N}{d\omega d\Omega} = \frac{\alpha \omega}{4\pi^2} \left| \frac{\mathbf{n}_s}{k_\mu^i u_0^\mu} \times \left(\mathbf{A}_0 + \mathbf{k}_i \frac{\mathbf{A}_0 \cdot \mathbf{u}_0}{k_\mu^i u_0^\mu} \right) e^{-ik_\mu^s x_0^\mu} \int_{-\infty}^{+\infty} \exp \left\{ -i\phi \left[1 - \frac{k_\mu^s u_\mu^0}{k_\mu^i u_0^\mu} \right] \right\} d\phi \right|^2; \quad (36)$$

the spectrum is proportional to $\delta(k_\mu^s u_0^\mu - k_\mu^i u_0^\mu)$, and the corresponding Doppler-shifted radiation wavenumber, expressed in vector form, is

$$k_s = \frac{\gamma_0 k_i - \mathbf{u}_0 \cdot \mathbf{k}_i}{\gamma_0 - \mathbf{u}_0 \cdot \mathbf{n}_s}. \quad (37)$$

We also note the presence of the term $e^{-ik_\mu^s x_0^\mu}$, which is related to the coherence of the radiation process.

This result can be obtained in a completely different way, by considering the correlation between the initial photon state and the scattered photon 4-wavenumber, as derived from the conservation of energy-momentum:

$$m_0 c u_\mu^0 + \hbar k_\mu^i = m_0 c u_\mu^s + \hbar k_\mu^s, \quad (38)$$

which can also be expressed as

$$u_\mu^0 + \tilde{\lambda}_c k_\mu^i = u_\mu^s + \tilde{\lambda}_c k_\mu^s, \quad (39)$$

after introducing the Compton wavelength, $\tilde{\lambda}_c = \hbar / m_0 c = r_0 / \alpha$. In addition, the 4-velocity is normalized, with $u_\mu u^\mu = -1$, and the photon mass shell condition, or dispersion relation, implies that $k_\mu k^\mu = 0$. Using the first condition, we have:

$$u_\mu^s = u_\mu^0 + \tilde{\lambda}_c k_\mu^i - \tilde{\lambda}_c k_\mu^s, \quad u_\mu^s u_s^\mu = -1, \quad (40)$$

which yields

$$\left[u_\mu^0 + \tilde{\lambda}_c (k_\mu^i - k_\mu^s) \right] \left[u_0^\mu + \tilde{\lambda}_c (k_i^\mu - k_s^\mu) \right] + 1 = 0. \quad (41)$$

Explicitly developing Eq. (41), we first find that

$$u_\mu^0 u_0^\mu + 2\tilde{\lambda}_c u_\mu^0 (k_i^\mu - k_s^\mu) + \tilde{\lambda}_c^2 (k_\mu^i - k_\mu^s)(k_i^\mu - k_s^\mu) + 1 = 0; \quad (42)$$

using the normalization of the 4-velocity, this reduces to

$$2\tilde{\lambda}_c u_\mu^0 (k_i^\mu - k_s^\mu) + \tilde{\lambda}_c^2 (k_\mu^i k_0^\mu - 2k_\mu^s k_i^\mu + k_\mu^s k_s^\mu) = 0; \quad (43)$$

finally, the dispersion relation allows us to eliminate the quadratic terms in $k_\mu k^\mu$, to obtain the sought-after relation between the initial and final photon states:

$$k_\mu^s (u_0^\mu + \tilde{\lambda}_c k_i^\mu) = k_\mu^i u_0^\mu. \quad (44)$$

Neglecting recoil, we recover the result derived using the well-known classical radiation formula. The close analogy between the two derivation methods suggests a straightforward extension of the radiation formula to include quantum recoil: instead of using a ballistic trajectory, the average recoil experienced by the electron along its trajectory is also taken into consideration, with

$$\frac{dx_\mu}{d\phi} = \frac{dx_\mu}{d\tau} \frac{d\tau}{d\phi} = \frac{u_\mu}{-k_\mu^i u_0^\mu} = \frac{u_\mu^0 + \tilde{\lambda}_c k_\mu^i}{-k_\mu^i u_0^\mu}, \quad x_\mu(\phi) = x_\mu^0 - \frac{u_\mu^0 + \tilde{\lambda}_c k_\mu^i}{k_\mu^i u_0^\mu} \phi. \quad (45)$$

The radiation formula reads:

$$\frac{d^2 N_s}{d\omega_s d\Omega_s} = \frac{\alpha \omega_s}{4\pi^2} \left| \frac{\mathbf{n}_s}{k_\mu^i u_0^\mu} \times \left(\mathbf{A}_0 + \mathbf{k}_i \frac{\mathbf{A}_0 \cdot \mathbf{u}_0}{k_\mu^i u_0^\mu} \right) e^{-ik_\mu^s x_0^\mu} \int_{-\infty}^{+\infty} \exp \left\{ -i\phi \left[1 - \frac{k_\mu^s (u_\mu^0 + \tilde{\lambda}_c k_\mu^i)}{k_\mu^i u_0^\mu} \right] \right\} d\phi \right|^2, \quad (46)$$

which leads to the correct radiation frequency.

The differential scattering cross-section, which can be traced back to the term

$$\left[\frac{\mathbf{n}_s}{k_\mu^i u_0^\mu} \times \left(\mathbf{A}_0 + \mathbf{k}_i \frac{\mathbf{A}_0 \cdot \mathbf{u}_0}{k_\mu^i u_0^\mu} \right) \right],$$

corresponds to the Lorentz-boosted classical Thomson

scattering cross-section. Indeed, when the electron is initially at rest, this term simplifies to $\mathbf{n}_s \times \mathbf{A}_0$; upon taking the square of the product and normalizing by the incident power density, the term $|\mathbf{n}_s \times \pi_i|^2$ is left, where π_i is the polarization of the incident wave.

In turn, this further suggests that the correct Klein-Nishina cross-section can be used by appropriately modifying the aforementioned cross-section term.

2.8. Classical limit of the Klein-Nishina formula

Comparing the two different formalisms that can be used to describe the interaction between a relativistic electron and a plane wave in terms of number of photons scattered per unit wavenumber and solid angle, we are now seeking to establish the classical limit of the Klein-Nishina formula:

$$\frac{d^2N}{dq d\Omega} = \frac{\alpha}{4\pi^2 q} \left| \mathbf{q} \times \int_{-\infty}^{\infty} \mathbf{u}(\tau) e^{-iq_\mu x^\mu(\tau)} c d\tau \right|^2, \quad (47)$$

$$\frac{d^2N}{dq d\Omega} = \frac{d\sigma}{d\Omega} \frac{\kappa}{k} \frac{\tilde{n}_\lambda(k)}{|dq_C / dk|} \left| \int_{-\infty}^{+\infty} n_\lambda[x_\mu(\tau)] c d\tau \right|_{k=k_p}. \quad (48)$$

Equation (48) yields:

$$\frac{d^2N}{dq d\Omega} = \int_{-\infty}^{\infty} \int_{-\infty}^{\infty} \frac{d\sigma}{d\Omega} \delta(q - q_C) n_\lambda[x_\mu(\tau)] \tilde{n}_\lambda(k) c d\tau dk. \quad (49)$$

Equation (47) can be generalized to describe the scattering process for nonlinear, three-dimensional, and correlated incident radiation; Equation (49) properly satisfies 4-momentum conservation, therefore accounting for recoil, and also includes QED corrections when using the Klein-Nishina differential scattering cross-section. The two approaches yield complementary information, but are mutually incompatible, and coincide only for Fourier transform-limited (uncorrelated) plane waves in the linear regime and in the limit where $\lambda_C \rightarrow 0$.

Here, α is the fine structure constant; $q_\mu = (q, \mathbf{q})$ is the scattered 4-wavenumber; $u_\mu = dx_\mu / cd\tau = (\gamma, \mathbf{u})$ is the electron 4-velocity along its trajectory, $x_\mu(\tau)$; q_C satisfies

the Compton formula; n_λ is the incident photon density; and \tilde{n}_λ is the normalized incident spectral density.

The incident 4-polarization is:

$$\varepsilon_\mu = \frac{1}{\sqrt{-A_\nu A^\nu}} \left(A_\mu - k_\mu \frac{A_\nu u^\nu}{k_\nu u^\nu} \right); \quad \varepsilon_\mu \varepsilon^\mu = -1. \quad (50)$$

The scattered 4-polarization is:

$$\pi_\mu = \left(0, \frac{\mathbf{n} \times (\mathbf{n} \times \boldsymbol{\varepsilon})}{|\mathbf{n} \times (\mathbf{n} \times \boldsymbol{\varepsilon})|} \right); \quad \boldsymbol{\varepsilon} = \frac{1}{\sqrt{-A_\nu A^\nu}} \left(\mathbf{A} - \mathbf{k} \frac{A_\nu u^\nu}{k_\nu u^\nu} \right). \quad (51)$$

In the limit where $\lambda_c \rightarrow 0$, the Klein-Nishina differential scattering cross-section reduces to:

$$\frac{d\sigma}{d\Omega} = r_0^2 \left(\frac{q}{\kappa} \right)^2 \left(\varepsilon_\mu \pi^\mu \right)^2. \quad (52)$$

This last result shows that we recover the well-known dipole radiation pattern, as in described by the Larmor radiation formula. This derivation illustrates the care that must be taken when dealing with the 4-polarization, and taking into account both covariance and gauge invariance.

Finally, it is of interest to note that in the regime of Velociraptor, where recoil accounts for a fraction of % of the total kinematics, the quantum effects are much more important in terms of frequency scale than in terms of intensity: the classical and Klein-Nishina cross-sections are virtually identical, but the spectra are distinctly shifted, as shown below. In such a case, nonlinear effects can be modeled adequately by using the modified radiation formula derived above.

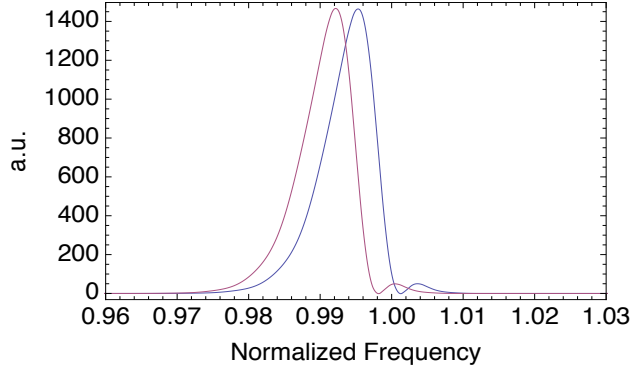


Figure 5 Comparison between Thomson (blue) and Compton (red) scattering spectra, on-axis. This case shows a mildly nonlinear ($A_0^2 = 0.01$), circularly polarized interaction.

3. Interaction simulations

In this section, we first present the formalism underlying the computer simulations used to describe the interaction between relativistic electrons, represented by macro-particles with charge-to-mass ratio, and an intense laser pulse. Parmela simulations of a high quality, 250 MeV, 250 pC electron bunch are illustrated below in terms of phase space. These phase space correlations are easily accounted for by the codes that have been developed to simulate the Compton scattering and benchmarked extensively against previous experiments.

Typically, head-on collisions are considered because they yield the maximum relativistic Doppler upshift and minimal sensitivity to timing and synchronization; in such situations, one obtains spectra that are accurately described by the product of a Gaussian and an error function (for Gaussian phase space distributions). Using the full electron beam phase space as an input to the simulations yields more detailed spectra, as illustrated in Fig. 11. In general, the asymmetric low energy contribution on-axis can be traced back to the electron beam emittance, which results in a distribution of crossing angles at focus: some electrons do not contribute their maximum Doppler upshift in the direction of observation.

In the case where the laser spectrum is narrow compared to other parameters ($\Delta\gamma/\gamma, \varepsilon_n$), brightness simulations can be performed efficiently by calculating the following quantities for each macro-particle:

$$\frac{r_0^2}{\sqrt{\pi} q (\gamma + u_z)^2 \Delta k}, e^{-\left(k_0 - q \frac{\gamma + u_z}{\gamma - u_z - 2q}\right)^2 / \Delta k^2}; \quad (53)$$

and replacing them by a Dirac delta-function with position and integral,

$$q = k_0 \frac{\gamma - u_z}{\gamma + u_z + 2k_0}, \quad \frac{r_0^2}{(\gamma + u_z)^2 k_0}. \quad (54)$$

In the specific case of Eqs. (53) and (54), the scattered radiation is on-axis, and the laser spectrum is a Fourier transform-limited Gaussian.

The calculation is finalized by calculating the dose radiated by each macro-particle, with total cross-section $N_e \sigma / N$, where N_e is the number of electrons and N is the number of macro-particles; by summing incoherently over all macro-particles; and by binning the result along the scattered frequency axis.

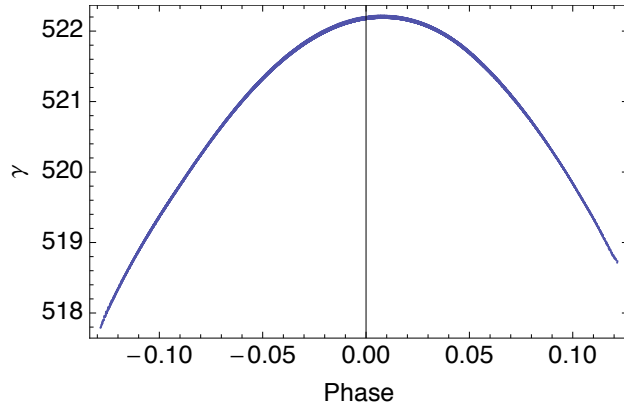


Figure 6 Correlation between the electron energy and rf phase.

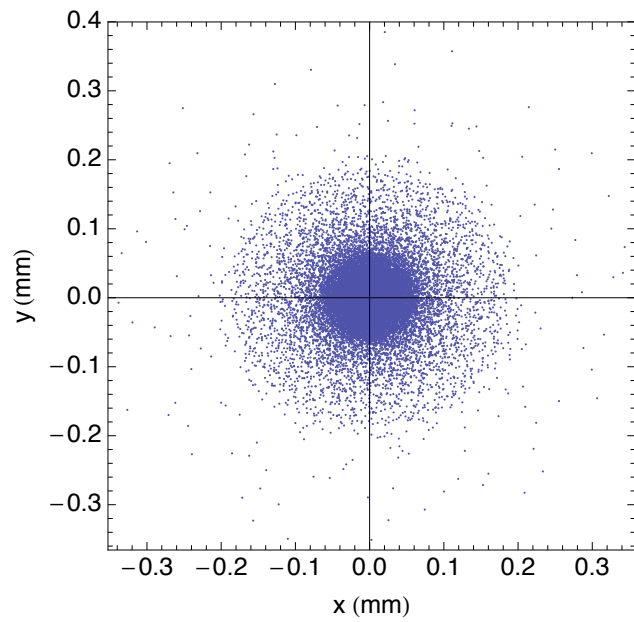


Figure 7 Focal spot for 0.25 nC, 250 MeV electron bunch.

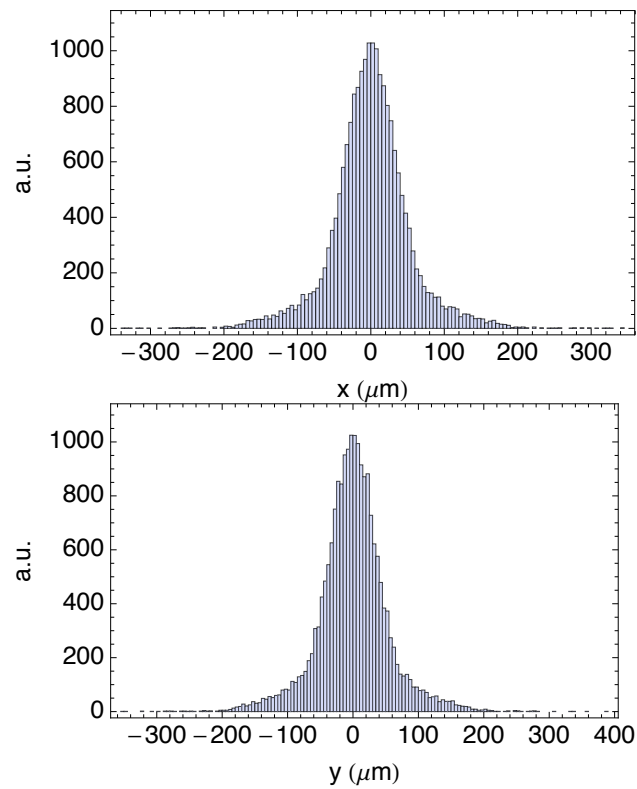


Figure 8 Histograms of the electron beam focus along the polarization (x-) axis and along the y-axis.

4. Parametric studies

Machine parameter sets are explored systematically, using the codes described in the previous section, in order to optimize our design. Particular emphasis has been paid to beam matching, as illustrated below.

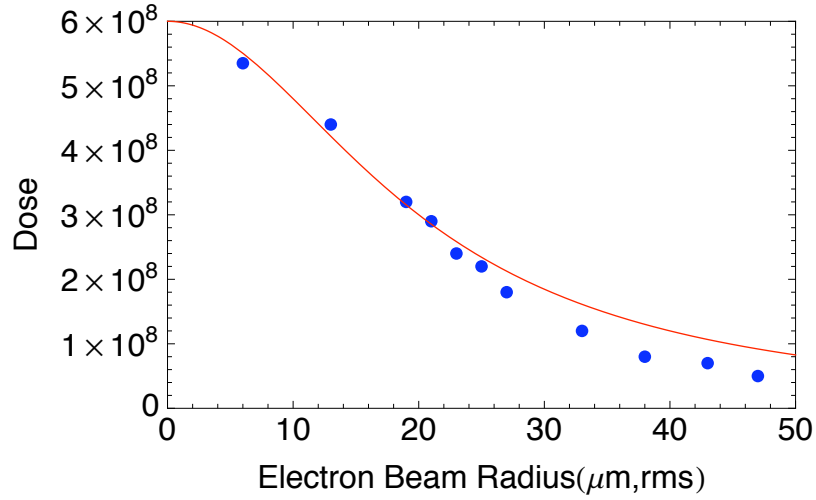


Figure 9 Dose (number of gamma-ray photons) as a function of the electron beam radius for a given laser focal spot (5 microns rms)

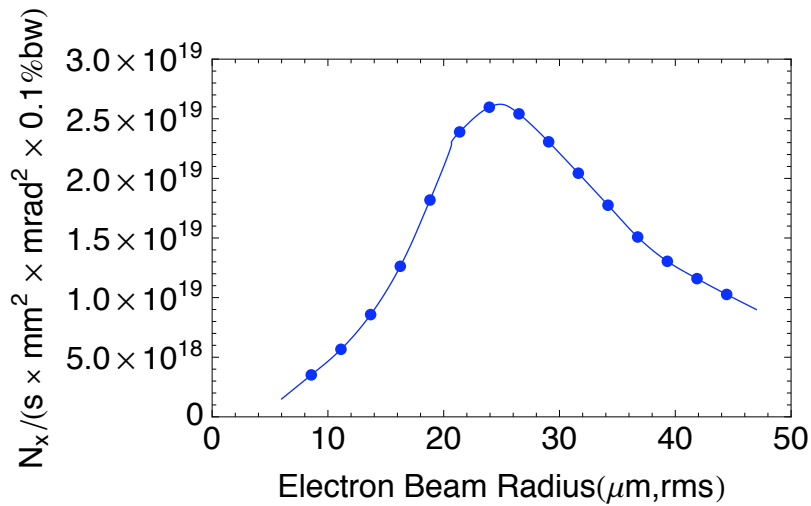


Figure 10 On axis peak brightness as a function of the electron beam radius for a given laser focal spot (5 microns rms)

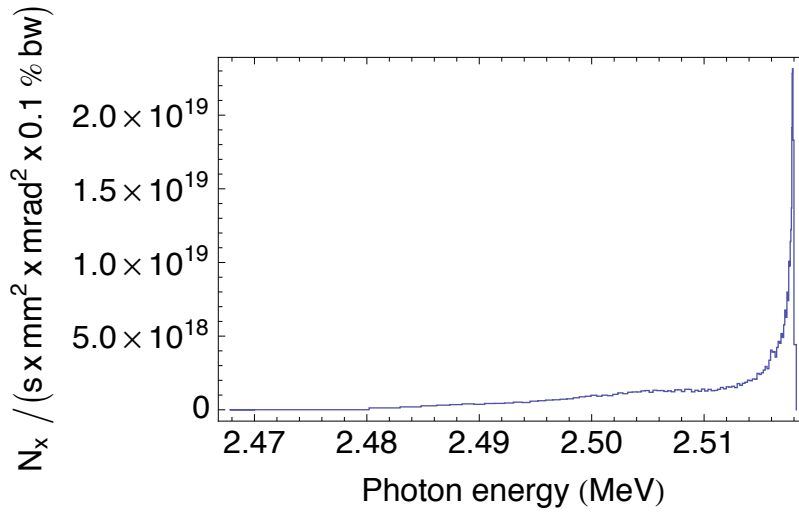


Figure 11 Example of a gamma-ray spectrum (for parameters see Table 1)

The main machine parameters are summarized below:

Gammas		Laser		Linac	
Energy	0.5/2.5 MeV	Wavelength	532 nm	Energy	250 MeV
Dose	10^8	Energy	0.5 J	Charge	0.4 nC
Spot	20 μm	Spot	20 μm	Spot	20 μm
Divergence	0.1 mrad	f:number	20	Emittance	1 mm.mrad
1/g	2 mrad	M ²	1.2	E-spread	0.2%
Duration	2 ps	Duration	10 ps	Duration	2 ps
Bandwidth	< 0.5%	Technology	DP Nd:YAG	Frequency	11.424 GHz
			HD CPA	Gradient	75 MV/m
Rep. Rate	120 Hz	Rep. Rate	120 Hz	Rep. Rate	120 Hz

Table 1 Key machine parameters.

5. Timing and synchronization

5.1. Mode-Locked, Phase-Locked Fiber Laser Oscillator

The fiber-based mode-locked, phase-locked oscillator developed for T-REX proved to be very reliable. Over the course of two years, it ran 24/7 with no unintended

interruptions in service. It did, however, suffer two shortcomings. It had a limited frequency tuning range (a limited ability to compensate for temperature drifts), and its spectrum barely covered the combined PLS and ILS spectral ranges.

The oscillator being built is very similar to the one used in T-REX, but will have several enhancements. It will implement the latest control circuitry (developed for NIF), it will have a broader frequency tuning range, and its spectrum will be shifted to longer wavelengths to better cover the PLS and ILS requirements. The spectrum will also be flattened with an external optical filter in order to mitigate self-phase modulation issues in the PLS, which now requires 0.3 ps pulses (less than half the T-REX duration).

5.2. Low Level RF and Synchronization

As with the previous systems we have developed, we will use the laser oscillator as the master clock. A reference crystal running at 40.8 MHz is used to keep the oscillator locked to approximately the right frequency. The laser pulse train is monitored with a photodiode and the signal filtered to produce the RF signal that is used to drive the photoinjector and accelerating sections. Because this same oscillator produces the light for both electron generation and electron scattering, using it as the reference allows us to maintain synchronization between the laser and the electron beam, even if the frequency of the oscillator drifts.

With the change in frequency from S-band to X-band, the requirements on RF phase stability increase. The laser must arrive at the photocathode within one RF degree (243 fs) of the proper accelerating RF phase to avoid degrading the emittance, which imposes stringent requirements on the phase jitter of the RF source. In the original low-level RF design, the signal from photodiode monitoring the pulse train was filtered to the fundamental frequency (40.8 MHz), and then frequency multiplied in a Phase-locked Dielectric Resonant Oscillator (PDRO) up to the 11.424 GHz operating frequency of the accelerator before being fed to the klystrons. An alternative scheme is to use a high-speed monitor diode and filter the resultant signal directly at the frequency to be used in the accelerator skipping the frequency multiplication step.

To determine whether the extra amplification required by the high-frequency filtering offsets any gains from not having to frequency multiply, we have procured the hardware

necessary to generate the RF using both methods, so we can determine which method has the lowest phase noise before selecting the scheme we will use in the system.

We have also begun looking into the issues involved in transporting the PLS pulse to the gun, and what timing jitter that might induce. One solution under study is to transport some of the 40.8 MHz signal along the same transport and generate the RF signal near the gun input, cancelling out any phase error that would have resulted from the transport line.

5.3. TWTA, phase and amplitude feedback

The X-band klystron XL-4 is an amplifier and needs an input RF driver. This RF driver consists of the low-level RF (LLRF) in the dBm power range and medium power driver in the kilowatt range. A travelling wave amplifier (TWTA) will be used to provide the medium power needed. A Teledyne MTI-3048D TWTA will be used. It can provide up to 2 kW of peak output power, which is sufficient to drive two to three XL-4 klystrons. A turnkey TWTA system (ETM 13PIJ) with power supply and pre-amp front end will be purchased. With this turnkey system and a RF feedback loop, we can achieve superior RF output pulse flatness and phase stability. Ripple compensating and RF correction is applied to the 11.424 GHz carrier, and subsequently to the input of TWTA, which in turn drives the klystron. This technique was shown to achieve RF output pulse flatness within 0.1% in similar system

6. High power RF X-band system

To obtain the desired electron beam with the energy needed for the resulting gamma ray wavelength, high power microwave/RF is needed to accelerate the electrons at the RF gun and the subsequent accelerating structures. As presently conceived, the RF gun would need about 16 MW of RF power and each accelerating structure would need 60 MW of peak RF power. The total peak power needed for 125 MeV electron beam would be about 200 MW. At our operating frequency 11.424 GHz (X-band), the proven high power RF source is the SLAC X-band klystron, the XL-4. The peak output power of XL-4 is 50 MW with a RF pulse length of 1.5 μ s at a repetition rate of 60 GHz. One XL-4 will be use to power the system. This is achieved with RF pulse compression scheme

called the SLEDII, developed for the Next Linear Collider project at SLAC. The present design would result in a power gain of 4 with a pulse length of 200ns. This will give us the 200 MW needed. The 200 MW, 200 ns pulse will then be distributed via high power, low loss power distribution system to the RF gun and each of the three accelerator sections.

6.1. Solid-State High Voltage Modulator

A high voltage modulator provides the high voltage pulse required by the klystron. In general, the modulator consists of charging power supply, pulse forming and switching system (pulse forming network with thyatron or solid state power switching power modules), high voltage pulse transformer, and the klystron socket. The performance of modulators based on solid-state technology far exceed that of PFN and thyatron based systems in terms of stability and repeatability. This is demonstrated by the system we have selected from ScandiNova. The amplitude stability can be $<0.02\%$. In this system, the dc power supply (DCPS) is the main power source of the system. It converts the 3-phase line voltage to a regulated DC voltage. It charges up all the IGBT Switching Modules to a primary voltage around 1000V. The IGBT's are high-power solid-state switches, which can be turned on and off electronically, responding to a gate pulse. When an external trigger pulse enters the modulator, it gates all the IGBT Modules and discharging them through the primary winding of a high voltage pulse transformer. The high voltage transformer step the 1 kV, high current pulse into the desired 420 kV pulse for the electron gun of the klystron. The modulator also provides the heater power to the klystron and all the ancillary requirements of the high power klystron amplifier including the solenoid and vacuum power supplies and water manifold to the klystron and the solenoid. It also consists of the control and interlocks for the modulator and the klystron.

6.2. SLAC XL-4 Klystron

The high power X-band source is a klystron amplifier. There has been years of research and development spent on the X-band klystron amplifier. However, the main focus of SLAC and the linear collider community had been the periodic permanent magnet (PPM) focusing klystrons. The reason is to save the power of the electromagnet, which

is 25 kW per klystron. For a 500 GeV linear collider, one would need approximately 3750 klystrons, which represents 100 MW of continuous magnet power.

Parameter	Quantity	Unit
Beam voltage	420	kV
Beam current	330	A
Perveance	1.2×10^{-6}	$A/V^{3/2}$
Frequency	11.424	GHz
RF output peak power	50	MW
RF pulse width	1.5	μs
Repetition rate	120	Hz
Gain	> 50	dB
Average RF power	9	kW
Focusing field	4.7	kG

Table 2 SLAC XL-4 klystron parameters.

For Velociraptor, we need two klystrons to accelerate the electrons to 250 MeV, the electron energy needed for our nuclear fluorescence resonance experiments. Hence, we would not mind using an electromagnet (solenoid) focusing klystron. The klystron amplifier chosen is the XL-4 klystron. This klystron has gone through extensive development and had been used extensively to test high gradient accelerator structures. In fact, these are the only working high power X-band klystrons in use at SLAC today. The main characteristics of the XL-4 klystron are listed in Table 2. The X-band klystron XL-4 is the most reliable high power X-band source today. It is capable of generating 50 MW of output power with about 400 watts of input power. Seven years of research and development and ten million dollars had been spent on developing the XL-4. The XL-4 finally was able to achieve >75 MW of peak output power at 100ns of pulse width. The keys to XL-4 success were TE01 mode output, strong focusing magnet (1.2 μ perveance 4.7 kG solenoid field), stainless steel drift tube, vacion pump at electron gun end, and travelling wave output circuit with four travelling wave output cavities.

6.3. SLED II Compression Line

The total output peak RF power of the two klystrons is 100 MW, which is not enough for accelerating the electrons to 250 MeV. However, the pulse length of 1.5 μ s is far too long. The logical step is RF pulse compression. This is done regularly at SLAC. In fact, the acronym SLED came from Stanford LINAC energy development program, later became Stanford LINAC energy doubling (SLED). The RF compression method we are going to use is SLED-II. It was developed to provide a level RF output by using traveling wave delay line instead of the RF cavities as in the original SLED. The output level of the RF output will be at the last round trip the traveling wave had completed. For example of a 250 ns output pulse length, the wave will be coupled out the 4-port hybrids after the fifth round trips by switching the phase of the RF output of the klystron. With the application of SLED-II, we hope to get an output power of 400 MW. This 400 MW will be distributed between the RF gun, which requires 16 MW, and six T53VG3MC accelerating structures.

6.4. High-Power X-Band RF Distribution

The entire high power RF compression and distribution system is operated under high vacuum. Gate valves are used to compartmentalize the different areas of the LINAC. In-line pump-out ports will be distributed throughout the system. These in-line pump-outs are co-axial pipes with pump-out holes, which are cut-off for the X-band RF on the inner pipe and connection to vacuum pump on the outer pipe. The RF distribution and diagnostics system can be divided into three parts, namely the klystrons, the SLED II, and the RF distribution. Each klystron generates 50 MW of peak RF power. This power will be fed to the SLED II pulse compression system. The output of the SLED is designed to have a power gain of four. This compressed pulse will be distributed throughout the system by hybrid, magic-Ts, phase shifters, and attenuators. RF loads will be used to terminate the 4-ports and the LINAC sections. The following diagram shows a schematic of the system. The output of the SLED II pulse compressor will be fed to a 4.8 dB hybrid. One third of the power will be going to the RF gun and first two LINAC sections. This 1/3 power will be further divided between the RF gun, which requires 10 MW and the first two LINAC sections, which will consume the rest. The

other 2/3 of the RF power will be equally divided between the last two parts of the LINAC, with two T53VG3MC in each part. Four port hybrids are used throughout the system to allow for flexibility and to have RF loads distribute throughout the system to absorb reflections.

7. High brightness X-band RF gun

7.1. Gun Design

The basic design and construction of a 5.5 cell photoinjector operating at 11.424 GHz is based on SLAC X-band RF gun experiment. This RF gun is unique in its design because of the number of cells used and its high operating surface field gradients: > 200 MV/m at the photocathode. The basic gun parameters are listed in the table below. The RF power for the RF gun and accelerator will be derived from a SLED-II pulse compressor powered by a 50 MW X-band klystron. The use of magic T, phase shifter and attenuator will permit independent phase and amplitude control of input to the RF gun. Improvement to this RF gun will be made in term of mode separation. This work is now in progress.

Number of Cells		5.5
Peak	surface	200 MV/m @
gradient/power		16 MW
RF filling time		65 ns
Cathode material		Cu
RF pulse length		200 ns
Mode separation		> 15 MHz
Field balance		< 1%

Table 3 X-band RF gun parameters.

7.2. Low Energy Beam Dynamics

The 250 MeV linac design begins with a 5.5 cell X-band photo-gun to be built by a collaboration between LLNL and SLAC. The gun design is based on a previous SLAC gun, which was operated with 200 MV/m peak accelerating field, and generated 0.5 nC, 7 MeV bunches. Beam parameters are chosen partially by scaling the design of the S-

band, T-REX (Thomson-Radiated Extreme X-rays) photoinjector. The ideal design scaling of lengths with λ_{RF} and fields with $1/\lambda_{RF}$ would require 480 MV/m electric field on the photo-cathode. In the present case, the beam plasma wavenumber, $k_p = \sqrt{4\pi r_0 n_e / \gamma^3}$, where r_0 is the classical electron radius and n_e is the beam density, is scaled with the increase in anticipated field strength from the S-band system (a factor of 5/3). To maintain an RF curvature induced energy spread of a few times 10^{-3} , the pulse length is set at 10 degrees of RF phase, scaled strictly with frequency. A bunch charge of 400 pC was selected with transverse size at the cathode chosen to produce the desired k_p . Also scaling with k_p is the drift distance from gun to linac section, chosen in this case to be 80 cm.

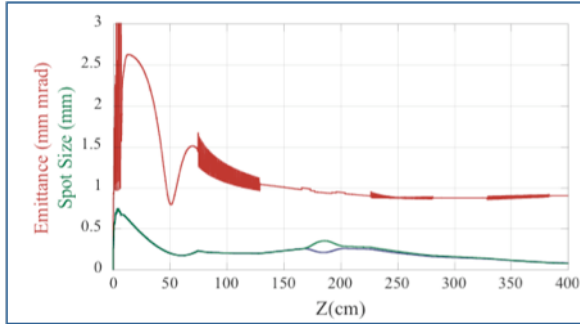


Figure 12 LEB Parmela simulation.

A Parmela simulation of the injector is shown in Fig. 12. The well developed emittance compensation technique is employed to produce an emittance minimum before injection into the first linac section where acceleration arrests the space-charge emittance oscillation at a second normalized emittance minimum of just under $1 \mu\text{m rms}$.

The drift region between the gun and first section, in addition to reducing the emittance, must provide an entry port for the cathode drive laser and is used to diagnose electron beam charge, size, steering, and gun phase for the 7 MeV beam injected into the first accelerator section. This Low-Energy Beamline (LEB) has been fully designed.

7.3. Photocathode laser system

7.3.1. Fiber Front End

The fiber front-end (seed source) includes the mode-locked oscillator (§5.1), and for the PLS, a preamplifier chain that includes a new type of preamplifier (described below), a fiber/bulk hybrid amplifier, and a fiber rod amplifier (§7.3.2). Throughout the front-end, amplified spontaneous emission is cleaned from between the pulses by acousto-optic and electro-optic modulators.

The first several fiber-based preamplifiers are based on miniaturized telecom-like components; they are essentially the same as those developed for T-REX. Combined, the telecom-like preamplifiers bring the pulse energy to 0.1 μJ at a repetition rate of 10 kHz. The telecom preamps are followed by a new type of preamplifier that can generate pulses having 4 x more energy than the telecom amps. This preamp, based on commercial components, will bring the energy to 4 μJ . The final preamplifier is followed by a fiber/bulk hybrid amplifier, similar to the one developed for T-REX; it will bring the energy to 100 μJ , roughly three times the T-REX level.

7.3.2. Fiber Rod Amplification

The T-REX fiber front-end was limited to pulse energies of roughly 50 μJ . The system being developed here will be able to achieve energies of 1 mJ, due to its new amplifiers: the 4 μJ preamplifier described in §7.3.1 and the rod-based amplifier described here.

The rod amplifier will be based on Yb-doped silica rods that support guided modes having diameters on the order of 65 μm . Researchers at the University of Jena have demonstrated that these can generate pulses having energies of 1 mJ at 100 kHz (100 W) that are compressible to 0.8 ps. In addition, in 2007 LLNL's fiber group demonstrated a rod-based 4 mJ system (30 ns, uncompressed) as part of a CRADA with an outside aerospace company.

The new system will be more demanding than past systems in that the compressed pulse lengths will be much shorter (0.3 ps) than the Jena work, and thus require low-ripple dispersion control over a very broad spectral bandwidth (20 nm vs. 4 nm). For this reason, the pulses will be stretched with bulk gratings rather than the Bragg grating-based stretcher that was used for T-REX (under T-REX, the Bragg stretchers were found to be ripple-prone).

7.3.3. Stretching, Compression and Quadrupling

The CPA based PLS system requires high fidelity pulse stretching and compressing. Prior experimental work and completed simulations indicate that a transform limited pulse is required for a properly synthesized waveform on the photocathode. Our simulations indicate that transform limited 360 fs (full width at $1/e^2$) duration pulses

(15 nm bandwidth) are necessary to meet the required specifications. This pulse will be stretched to 3 ns prior to amplification to avoid damage and reduce nonlinear phase accumulation. The corresponding stretcher bandwidth is 20 nm to reduce spectral clipping. After stretching, we will flatten the pulse spectrum with a custom designed spectral filter, amplify, and finally apodize the spectrum to further mitigate nonlinear phase accumulation. The required compressor bandwidth is 18 nm. Our calculations indicate that 238 ps/nm pulse dispersion is required in the stretcher and in the compressor.

Our prior work on T-REX indicates that fiber based CFBG stretchers do not always allow high fidelity pulse recompression. We have therefore considered several bulk stretcher designs. The standard Treacy-type design utilizes a relay-imaging lens. The grating is then placed inside the relay plane to introduce positive dispersion. The lens-based stretcher suffers from significant chromatic and geometric aberrations for large (10000 x) pulse stretching factor required for our system. Therefore, we are designing an all-reflective Offner-type pulse stretcher.

The stretcher utilizes 1740 grooves/mm gratings at 5 degrees off Littrow angle and forms a compact footprint (8' x 2'). Both the input and the output beam to the stretcher will be fiber coupled.

The pulse compressor is a standard Treacy-type design based on large area multi-layer dielectric gratings for high throughput efficiency. The compressor will be double passed to reduce the total footprint (8' x 2'). It will utilize higher groove density gratings to compensate for material dispersion in the amplifier. The angle of incidence will be adjusted based on the FROG measurements of the compressed pulse.

After the compressor, the pulse will be frequency quadrupled using two BBO crystals in Type I – I phase matching configuration. We expect 10-20% conversion efficiency from 1053 nm to 263.25 nm. The overall conversion efficiency is limited by temporal pulse walk-off and 2-photon absorption in the UV.

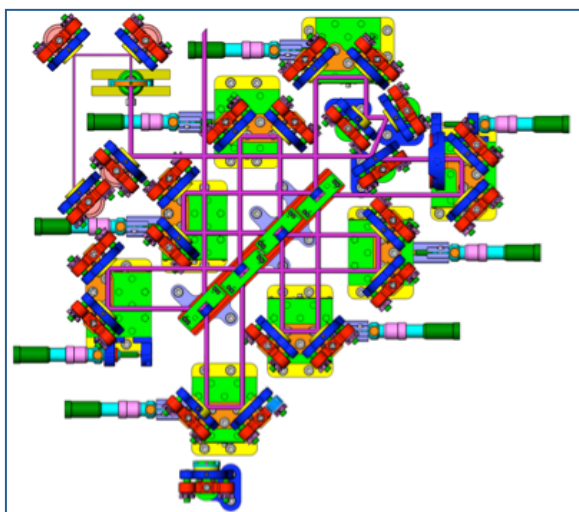
In the previous system, we learned that the chirped fiber Bragg grating technology we used, though promising, hasn't yet fully reached the point where it can be reliably integrated into a large scale system like the source we are developing. Thus, we are designing a matched bulk optic stretcher and compressor pair. Simulations of the laser,

including both harmonic generation effects and pulse stacking interference (discussed below), indicate that about 15 nm of laser bandwidth is needed at the fundamental frequency to produce pulses that have the desired fast rise time and minimize inter-pulse interference after stacking. The compressed 1053 nm laser pulse generated will then be propagated through two frequency-doubling stages to generate 50 μ J of 263 nm photons capable of extracting electrons from the photoinjector cathode. The pulse can then be shaped and delivered to the photoinjector

7.3.4. Spatio-Temporal Shaping

The PLS pulse shape requirements are driven by the performance of the photoinjector. Simulations show that the ideal shape is a 8-10° flattop pulse with very fast rise and fall times ($\leq 1^\circ$). To generate this pulse shape, we will use a pulse stacker to convert a single short pulse into eight closely spaced pulses. There are two ways being examined to do this.

The first method used in the T-REX project, is to use the “hyper-Michelson pulse stacker” concept. In this scheme, the laser pulse passes through a series of beam splitters, each time being recombined following an adjustable delay path. Three splitters will create eight pulses. Although this method allows for easy adjustment of the inter-



pulse spacing, the relative intensities of the separate pulses is set by the coatings on the beam splitters and is not easy to adjust. The intensities are easy to measure, however, because any single pulse can be passed while blocking the others.

The second stacking option is to use a series of birefringent crystal. Two different

Figure 13 Hyper Michelson pulse stacker

polarizations of light have different propagation times through the crystals, so the crystal lengths set the pulse spacing and therefore not easy to adjust once the crystals are in

place. The relative intensities of each pulse is easily adjusted by rotating the crystals, though measuring the individual pulse intensity requires a temporal diagnostic since individual pulses can't be blocked.

In either case, limits to the beam flatness derive from interference effects between consecutive pulses. Simulations of this effect show that pulse interferometric stability and modulation of the pulse intensity in time have to be balanced. To measure the actual laser pulse, we will use the same cross-correlator scheme demonstrated with the T-REX laser, mixing residual 1ω light with the 4ω light to generate 3ω light and measure the temporal profile of the pulse being delivered to the photocathode.

The pulse also needs to have a flat transverse profile with sharp edges. In T-REX, this was done by simply clipping the Gaussian profile with a round aperture and imaging the resultant profile on the photocathode. Although this works quite well, it is very inefficient, throwing away >70% of the laser energy. We are examining options to use a high-throughput spatial beam shaper to convert the profile from Gaussian to flat.

8. 0.25 GeV X-band linac

The accelerator uses 6 X-band traveling-wave sections of type T53VG3, developed by SLAC in a program for International Linear Collider structure R&D. These 60 cm, $2\pi/3$ phase advance per cell structures are simulated with an accelerating gradient just below 80 MV/m, limited by anticipated RF power availability. Although Fig. 10 shows the beam evolution through only three sections, the emittance and spot sizes are essentially unchanged by the following sections, and the simulated final beam energy is 267 MeV.

8.1. T-53 Accelerating Sections

SLAC had made great progress in understanding high-gradient performance in X-band structure during the Next Linear Collider project. The advances result from an aggressive experimental program, which had included the completion of tests of three pairs of low group traveling wave structures (T-series), an initial test of a pair of high phase advance traveling wave structures (H-series), and operation of three pairs of standing wave structures from 1996-2004. Most significant, however, has been the achievement of the NLC design gradient of 70 MV/m in a 53-cm, 3% c structure that has

been measured with 400-ns pulses for many hours at 73 MV/m with a breakdown rate of about 0.04/hour and at 85 MV/m with a breakdown rate of 0.5/hour. This is the T53VG3MC accelerator structure, which we are going to employ in Velociraptor. The combination of mode converter input structure (MC) with low group velocity (3% group velocity, VG3) has resulted in a remarkable reliability if operated in 70 MV/m range as seen in the result. We can employ up to six T53VG3MC structures in our accelerator depending on how many klystron and modulator unit we have.

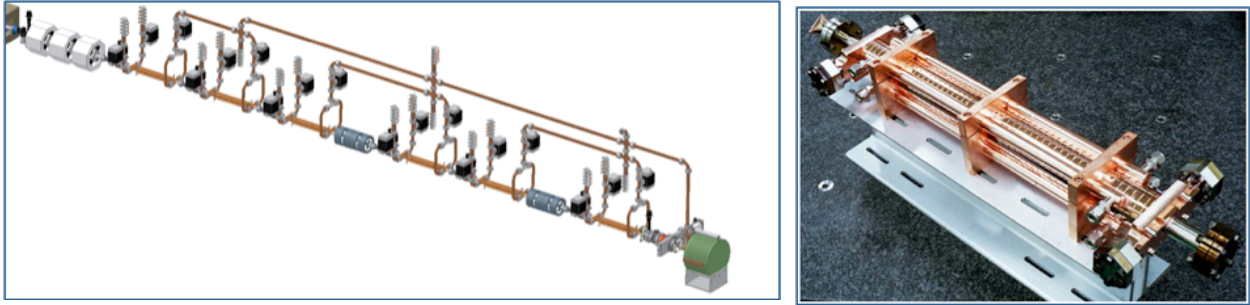


Figure 14 X-band linac architecture and X-band accelerating section.

8.2. Lattice and Linac Expected Performance

The key issues addressed in the design of the beam transport lattice from the exit of the linac to the Compton-scattering IP are emittance preservation, mitigation of on-axis Bremsstrahlung, and incorporation of the interaction laser into the final-focus optical system. In previous Compton source development work at LLNL, unwanted background radiation limited the utility of many of the γ -ray beam diagnostics employed. This radiation was observed to be effectively on-axis (i.e., only partially removed by collimation), unchanged by absence of photo-beam, and eliminated by removing RF power in the photo-gun. Spectral measurements were performed using a high-purity Germanium detector, which showed the radiation to be broadband, and extending upwards of 8 MeV (detector range limited). From this evidence, the noise source is determined to be Bremsstrahlung produced by dark current electrons generated in the gun and striking the walls of the accelerator and vacuum system downstream.

The increase in photo-cathode peak field in the planned machine, and its associated increase in dark current, makes the removal of the anticipated on-axis Bremsstrahlung an important lattice design consideration. The dogleg and chicane geometries have

been examined. Both the dogleg and chicane beamlines offer methods to shield radiation on the linac axis, while terminating dispersion-free ($\eta = \eta' = 0$). While the dogleg design offsets the γ -ray beam from the linac axis, and offers better potential for shielding, it is less compact, requires strong focusing, and is operationally less robust than the chicane. The chicane also has the advantage that it can be disabled to allow straight through operation if desired. While either lattice may be used for bunch compression, this design focuses on emittance preservation.

To investigate the effect of coherent synchrotron radiation (CSR) on emittance in these two cases, phase space distributions were taken from Parmela simulations of the linac and fed into the code ELEGANT. In the simulation of both systems a quadrupole triplet is inserted after the final linac section for proper matching into the bend lattice. Two more sets of focusing triplets follow, the last providing the final focus to the IP. The final bend plane (x) emittance increases slightly with inclusion of CSR in the simulation from 1.4 to 1.9 $\mu\text{m rms}$. This growth can be seen as an asymmetric tail in the configuration space.

Two different chicane geometries were simulated, the first using a 2 meter radius of curvature, 15° bends, and the second using 3.09 meter radius and 7° bends. In each case a 15 cm drift is set between the center magnets for insertion of on-axis shielding material. In the case with larger bend angles there is significant CSR induced emittance growth to 3.2 μm , while for the smaller chicane, no emittance growth is observed. The advantages of chicane beamlines mentioned above and effective emittance preservation of the small chicane motivate use of this design over the dogleg.

8.3. Jitter and Alignment

As mentioned above, round mean square position and pointing jitter should not exceed roughly 20% of respective bunch dimensions at the IP to avoid appreciable decrease in the photon source brightness. In the cases considered here, the IP sizes are $\sigma_x = 20 \mu\text{m}$, and $\sigma_x' = 0.2 \mu\text{rad}$, indicating a desired jitter below 4 μm and 40 μrad , respectively. A series of ELEGANT simulations has been performed to determine the effect of various random errors on the beam first and second moments at the IP. Jitter in beam position and pointing at the lattice entrance, ground motion induced jitter in magnet

position, and magnet misalignments were all simulated in batch runs of 400 to give 5% statistics on the resulting jitter figures. The simulations show that beam pointing stability from the accelerator is required to be on the order of $1\mu\text{rad}$. This can be accomplished with 10^{-3} linac energy jitter and steering due to misaligned elements kept on the order of 1 mrad.

8.4. Chicane Design and Simulations

The key issues addressed in the design of the beam transport lattice from the exit of the linac to the Compton scattering IP are emittance preservation, mitigation of near-axis Bremsstrahlung, and incorporation of the interaction laser into the final-focus optical system. In previous Compton source development work at LLNL, unwanted background radiation limited the utility of many of the γ -ray beam diagnostics employed. This radiation was observed to be effectively on-axis (i.e., only partially removed by collimation), unchanged by absence of photo-beam, and eliminated by removing RF power in the photo-gun. Spectral measurements were performed using a high-purity Germanium detector (HPGe), which showed the radiation to be broadband, and extending upwards of 8 MeV (detector range limited). From this evidence, the noise source is determined to be Bremsstrahlung produced by dark current electrons generated in the gun and striking the walls of the accelerator and vacuum system downstream. The increase in photo-cathode peak field in the planned machine, and its associated increase in dark current, makes the removal of the anticipated on-axis Bremsstrahlung an important lattice design consideration. The dogleg and chicane geometries are examined here. Both the dogleg and chicane beamlines offer methods to shield radiation on the linac axis, while terminating dispersion-free ($\eta = \eta' = 0$). While the dogleg design offsets the γ -ray beam from the linac axis, and offers better potential for shielding, it is less compact, requires strong focusing, and is operationally less robust than the chicane. The chicane also has the advantage that it can be disabled to allow straight through operation if desired. While either lattice may be used for bunch compression, this design focuses on emittance preservation. To investigate the effect of coherent synchrotron radiation (CSR) on emittance in these two cases, phase space distributions were taken from Parmela simulations of the linac and fed into the code

ELEGANT. In the simulation of both systems a quadrupole triplet is inserted after the final linac section for proper matching into the bend lattice. Two more sets of focusing triplets follow, the last providing the final focus to the IP. The simulated beam sizes and final focus configuration space is shown for the dog-leg geometry

Two different chicane geometries were simulated, the first using 2-meter radius of curvature, 15° bends, and the second using 3.09-meter radius and 7° bends. In each case a 15 cm drift is set between the center magnets for insertion of on-axis shielding material. In the case with larger bend angles there is significant CSR induced emittance growth to 3.2 μm , while for the smaller chicane, no emittance growth is observed. The advantages of chicane beamlines mentioned above and effective emittance preservation of the small chicane motivate use of this design over the dogleg.

9. Interaction laser system

The purpose of the Interaction Laser System (ILS) is to deliver Joule-class 532-nm pulses (the 2nd harmonic of Nd:YAG) to the interaction region at a 10-Hz rate, synchronous with the photoinjector and linac. Importantly, the nominally picosecond duration achievable with Nd:YAG (limited by the available gain bandwidth) is much better suited for the generation of narrow-band x-rays than sub-picosecond pulses. The system consists of a seed source phase locked to the photo-cathode drive laser (PLS), a three-head flashlamp-pumped Nd:YAG power amplifier, and a unique hyper-dispersion pulse compressor. The output from the pulse compressor is relay-imaged to the frequency-doubling set-up.

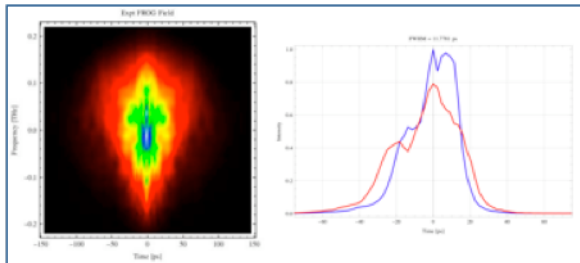


Figure 15 ILS Frog.

The ILS system has been developed under the T-REX SI. It suffered from poor pulse recompression and high wavefront aberrations that degraded beam shape at the focus. Substantial work has been completed to understand and correct these problems. We learned that poor pulse

recompression was caused by the chirped fiber Bragg grating (CFBG) stretcher. The CFBG exhibited group delay ripple, modulating the stretched pulse waveform. At high

enough amplifier gain, this modulation completely destroyed the seed pulse through nonlinear phase accumulation. In the linear regime, more than 70% of the energy in the recompressed pulse was scattered in a wide 400 ps pedestal.

We designed and tested a novel bulk hyper-dispersion pulse stretcher, which resolved pulse recompression problems. We also determined the main causes of poor spatial beam quality of the T-REX ILS system. The focusing problems were primarily caused by beam clipping in the compressor mirrors, the uncorrected astigmatism before the pulse compressor, and by beam aperturing in the amplifier rods. We completed a re-design of the ILS system to correct the spatial beam quality and increase the output pulse energy.

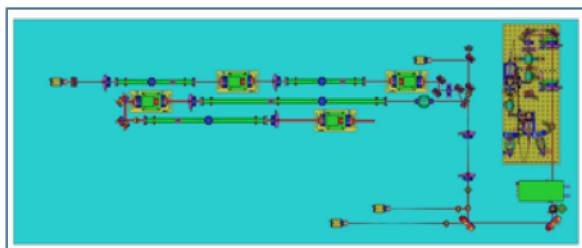


Figure 16 Redesigned ILS amplifier.

The redesigned system is shown in Fig. 16. The beam is relay imaged from the fiber output to each of the amplifier heads through a series of relay telescopes to improve beam quality and reduce thermal birefringence effects. Pointing and centering loops compensate for beam drift. A serrated

aperture is installed prior to Nd:YAG amplifiers to generate a high order super Gaussian beam. This increases the rod fill factor and improves spatial beam quality by eliminating beam ringing. Finally, a static phase plate will correct for any residual beam aberrations prior to the compressor.

9.1. Fiber Front End

The fiber front-end for the ILS is essentially the same as the one developed for T-REX, and is very similar to one that will be developed for the PLS (§7.3.1). The pulse repetition rate of the existing system, 10 kHz, already exceeds the new requirement of 120 Hz. Moreover, the pulse energy of the existing system, 30 μ J, is already sufficient to seed the ILS's new bulk amplifier; the latter is being developed with separate funds.

9.2. Hyper-Dispersion CPA

Chirped-pulse amplification in Nd:YAG with nanometer bandwidths is impractical using traditional two-grating pulse compressors due to the considerable spacing (~ 30 -m)

required between the gratings. We utilize a proprietary cascaded-grating “hyper-dispersion” architecture to provide the necessary dispersion (~ 3000 ps/nm) in a compact meter-scale compressor.

Conceptually, our design uses four multi-layer dielectric (MLD) diffraction gratings in a double-pass configuration. The use of MLD gratings allows high throughput efficiency of the compressor despite a total of eight grating reflections. The beam is incident near the Littrow angle on all of the gratings. The first grating reflection angularly disperses the incident collimated beam. In traditional two-grating compressors, the second grating collimates the dispersed beam. In our hyper-dispersion design, the second grating is oriented anti-parallel to the first grating, which additionally disperses the incident beam. The third and fourth gratings are arranged parallel, respectively, to the second and first gratings and collimate the spatially chirped beam.

The hyper-dispersion compressor has been designed and used in T-REX. The main upgrades will include better wavefront quality mirrors and a simplified 6-mirror retro-reflecting assembly. We are also exploring the option of spectral sculpting prior to the bulk amplifier to compensate for square pulse distortion.

9.3. Frequency Doubling

Frequency with large aperture Type II DKDP crystals has been demonstrated on T-REX with the bulk stretcher. The peak conversion efficiency was 40%. We will utilize a similar conversion scheme.

With the improved spatial beam quality and a properly optimized crystal thickness, we expect to achieve up to 50% conversion efficiency. We will also examine several alternate nonlinear materials, such as YCOB and LBO to handle higher average power.

9.4. ILS Diagnostics

New diagnostics are envisioned for the ILS system. The major difference here is that the data collection will be more centralized and integrated with the computer control system. Continuously acquired data will be logged and stored for future retrieval. Our plan is to install sufficient diagnostics for rapid system turn on and quick assessment of any potential problems. The pulse energy and beam profile will be monitored at all

control points in the system using energy meters, photodiodes, and CCD cameras. In addition, we will also measure the pulse spectrum after the stretcher and after the compressor.

We will also have several off-line diagnostics, such as pulse cross-correlator at 532 nm and pulse auto-correlator at 1064 nm. Pulse measurement of picosecond scale pulses is difficult. Its bandwidth is too narrow for commercial GRENOUILLE device and its pulse duration is too short to be measured directly with the oscilloscope. We have constructed a multi-shot FROG device for pulse measurement. A high-resolution $f = 1.5$ m spectrometer monitors the 2ω signal at the output of the auto-correlator. As the delay arm of the auto-correlator is varied, we obtain a 2D spectrogram of Intensity vs. time and frequency. This spectrogram can then be processed to yield the electric field vs. time of the pulse. A sample FROG measurement of the ILS pulse is shown in Fig. 16.

9.5. Interaction Region

Once the photons and electrons beams have been optimized, what remains is to bring them together at the interaction point to generate the final gamma ray beam. This requires careful design to ensure we are able to properly align the two beams in both space to approximately 10 μm accuracy, and in time to approximately 10 ps accuracy, without compromising the beam quality. The design for the Velociraptor interaction builds on our experience with previous interaction point designs. Those designs consisted of a set of focusing magnets for the electron beam and a dipole after the interaction to deflect the beam away from the gamma ray path. The laser had a long (~ 2 m) focal length, and passed through the dipole to reach the interaction point before being dumped down the length of the linac.

9.5.1. Electron Beam Matching

In the current design, the electron beam will be focused by a set of quadrupole magnets as before, but will now be re-collimated after the focus by a matching set of quadrupoles. The beam will then be deflected by a dipole and sent to a beam dump. The controlled collection of the electron beam will allow for the possibility of more advanced post-interaction diagnostics, or a more careful dump design (e.g. using a

decelerating section to reduce the beam energy before dumping) in the future. Parmela simulations have been done of electron beams with an emittance of 0.7 mm.mrad (an ideal case) and 3.0 mm.mrad (a worst case scenario), respectively, and have shown spot sizes on the order of 20 μm *rms* in both cases. The spot size can also be increased to examine experimentally the trade-off between electron density (which affects total flux) and beam divergence (which affects spectral width).

9.5.2. Laser Beam Matching

The laser beam, instead of having a long focal length and entering the interaction region through the final dipole, will be injected and collected via mirrors between the electron quadrupole sets. The mirrors will require holes to pass the electron beam. Simulations of the laser focus show that focal spots with sub-10 μm *rms* sizes are achievable with this geometry. Since the design includes a collection optic for the laser, integrating a laser pulse recirculation scheme in the future would be fairly straightforward.

9.5.3. Final Focus Design and Integration

We are working on upgrades to the Compton scattering codes to include the true propagation of the laser beam through the focus, replacing the simple Gaussian distribution currently used, to optimize the interaction geometry (parameters such as the focal length and spot size) to maximize the gamma ray brightness and properly include the effects of having a beam with a hole in the center, required for the on-axis optics.

9.5.4. IP Diagnostics

For alignment, we intend to include the same motorized alignment cube concept used successfully in the previous systems. Aligned at 45° to the beam axis, the cube reflects the focused laser light and generates optical transition radiation from the electron beam, allowing the positions of both beams to be observed simultaneously. The light from the cube will be also be imaged into a streak camera, allowing us to establish the necessary temporal overlap. In addition to the cube, we are looking at other alignment aids to help guarantee the overlap spatially. Due to difficulties in producing and maintaining a sufficiently precise edge to the cube, we can affix a thin metal plate with a small hole to the bottom of the cube. By observing the cube from both sides, we can center both

beams on the hole to establish the spatial overlap at the focus. By centering the electron beam on the holes in the laser mirrors, we also establish the alignment of both beams at two points 40 cm away from the interaction (80 cm total length), ensuring that the two beams are truly collinear to maximize the total scattered radiation.